

# Processes Controlling the Thermal Regime of Saltmarsh Channel Beds

KEVAN B. MOFFETT,<sup>\*,†</sup>  
SCOTT W. TYLER,<sup>‡</sup>  
THOMAS TORGERSEN,<sup>§</sup> MANOJ MENON,<sup>‡</sup>  
JOHN S. SELKER,<sup>||</sup> AND  
STEVEN M. GORELICK<sup>†</sup>

*Department of Geological and Environmental Sciences, Stanford University, Braun Hall, 450 Serra Mall, Stanford, California 94305-2115, Department of Geological Science and Engineering, University of Nevada-Reno, Reno, Nevada, Department of Marine Sciences, University of Connecticut, Groton, Connecticut, and Department of Biological and Ecological Engineering, Oregon State University, Corvallis, Oregon*

*Received June 3, 2007. Revised manuscript received October 5, 2007. Accepted November 19, 2007.*

Spatially and temporally continuous temperature measurements were collected over 32 h using a fiber-optic distributed temperature sensing (DTS) system deployed along 330 m of two intertidal saltmarsh channel beds in northern California. Measured temperature gradients imparted ecosystem-scale structure to the saltmarsh tidal channel thermal regime, which was punctuated by potential warm and cold refugia. Anomalous bed temperatures of 2–4 °C occurred throughout the 1.3 tidal cycles at some locations. Discrete locations of consistently warm temperatures characterized sustained seepage of recently infiltrated tidal waters. Low-variance temperature anomalies were typically collocated with hidden microtopographic tributaries that facilitated mixing of warm surface waters and cold groundwater. Bed temperature gradients (~2 °C/100 m, average) decreased from high temperatures similar to bay water at the channel mouths to low inland temperatures comparable to groundwater. The trends were maintained by cold groundwater discharge throughout the channels, which affected bed temperatures in proportion to channel reach exposure time; the opposing effect, conductive bed-warming by tidal waters, was proportional to flood duration. DTS is a promising tool for identifying spatial and temporal temperature patterns of hydroecological importance amidst complex natural systems.

## Introduction

Surface water–groundwater exchange is a fundamental feature of the physical, chemical, and biological systems constituting the coastal zone. Effects of this exchange include tidally induced water table overheight (1); marine nutrient loading (2, 3); and salinity, mineral, and isotopic alterations of terrestrial and near-shore waters (4, 5). Borehole temperature measurements have been used to identify off-shore

ocean–aquifer hydraulic connections (6), calculate coastal groundwater flow rates (7), and estimate submarine groundwater discharge (8) at point-locations. Thermal-infrared imaging can cover a broad area but is temporally discrete and can detect only the surface expressions of thermal anomalies related to groundwater–surface water mixing (9–11). Identification of exchange fluxes in the intertidal zone is complicated by variable degrees of tidally forced mixing between surface water and groundwater (12) and the tidally variable interfacial surface area and volume of surface water in the system. Although the heat balance of intertidal mudflats has been well-analyzed (13), there is a dearth of literature on the thermal regime of intertidal channels.

The hydroecological significance of variable intertidal sediment temperatures is indicated by a few studies. The presence of at least one species of benthic invertebrate is correlated with locally low temperatures and salinities of intertidal groundwater seeps (14). The use of cool thermal anomalies as refugia by Chinook salmon is well-established (15), while juveniles use intertidal channels as foraging access and refugia (16). The brackish tidal creek adjacent to this study's site supports anadromous salmonid runs (17). This study monitored a fiber-optic distributed temperature sensing (DTS) system installed in the bed of two intertidal saltmarsh channels to determine the spatial frequency and scales of occurrence of such thermal microhabitats and their relationship to groundwater discharge.

DTS provides distinct advantages over point-measurements in the field, including the following: spatially and temporally continuous measurement; integration as a single unified system, obviating separate calibration of multiple instruments; flexible deployment options (see ref (18) for diverse examples); very fast thermal response (through <4 mm of PVC-and-steel cable jacket) compared to many bulkier temperature loggers; fine spatial resolution (1.0 linear-meter, or centimeters if coiled (18)); and extraordinary temperature accuracy, to 0.01 °C in some cases. Applications of DTS to surface water hydrology have begun to test its response to transient surface water conditions (18) and surface water–groundwater interactions in freshwater streams (19); this study tested the utility of DTS in intertidal channels, a fundamentally different physical system.

## Materials and Methods

An extensive discussion of DTS physics is provided by Selker et al. (18). The DTS system used in this study emitted a 10-ns laser pulse into glass optical fiber and measured the Raman Stokes and anti-Stokes backscatter signals caused by photons gaining or losing energy during scattering. The two Raman peaks are symmetrical in frequency about the Rayleigh peak, which occurs at the same frequency as the laser source (~1050 nm in this study). The intensity of the higher-frequency anti-Stokes signal is strongly temperature-dependent since the number of photons that gain energy through scattering depends on the fraction of high-energy molecules in the optical fiber, i.e., its temperature. The ratio of the Stokes and anti-Stokes signal intensities may be calibrated to known temperatures for a given cable; we calibrated a 500-m length of 50/125-multimode optical fiber with constant-temperature water baths.

Based on the known speed of light in the cable, consecutive portions of the Raman signal following a DTS laser pulse can be assigned to successively distant backscatter origin locations within the cable. In this experiment the DTS system was programmed to initiate laser pulses every 30 s and to

\* Corresponding author phone: (650) 725-8070; fax: (650) 724-0979; e-mail: moffett@stanford.edu.

<sup>†</sup> Stanford University.

<sup>‡</sup> University of Nevada-Reno.

<sup>§</sup> University of Connecticut.

<sup>||</sup> Oregon State University.

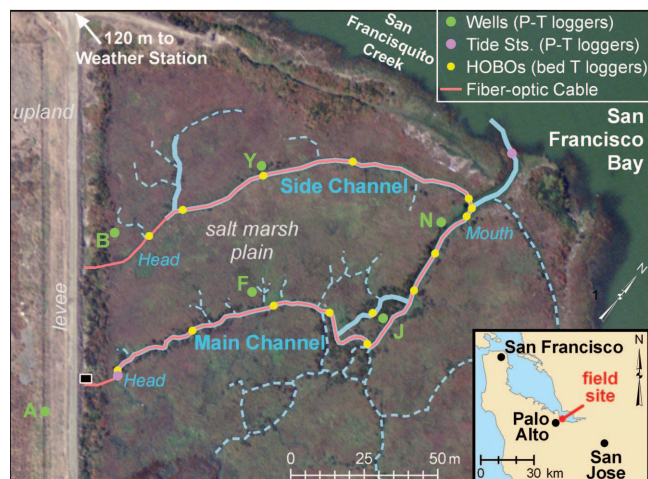


**FIGURE 1. Field site map, including position of cable in tidal channels and locations of supplementary data collection. Dashed blue lines are microtributaries known *a priori*.**

record the average temperature calculated from the backscatter originating within each 1.0-m interval of the cable following each pulse (1.0-m  $\times$  30-s resolution). Measurements were made only in one direction. The data were postprocessed by averaging over 10-min intervals to improve the signal-to-noise ratio according to calculations of the standard deviation/temporal averaging tradeoff. The calculated precision of the postprocessed data reported in this document is 0.7 °C (one standard deviation, at 1.0-m  $\times$  10-min resolution).

The study site comprised 1.8 ha of historical saltmarsh on the edge of San Francisco Bay in the Palo Alto Baylands Nature Preserve (37°27'54" N, 122°6'58" W). The fiber-optic cable was deployed in the two primary tidal channels (Figure 1). The main tidal channel is 177 m long from mouth to head and the side channel is 155 m long. The average marsh plain elevation is 1.25 m above mean sea level (aMSL); the base level of the main channel mouth is mean sea level. Data were collected between neap and spring tides during a maximum tidal range of 2.89 m. Tidal channels were empty during the lower half of the tidal cycle, apart from small rivulets of drainage, and the marsh plain was under  $\sim$ 0.3 m of water at high tide. The tidal channels are approximately rectangular in cross-section with width-by-depth measurements (m) as follows: main channel mouth (2.4  $\times$  1.3) and head (1.0  $\times$  0.8); side channel mouth (1.2  $\times$  1.2) and head (0.7  $\times$  0.1). The marsh plain includes microtopographic channels ( $\sim$ 0.1  $\times$  0.05–0.5 m) hidden beneath the vegetation and some larger tributaries (Figure 1).

Poorly consolidated estuarine clayey-silt prevails to a depth of at least 4 m (20), with a hydraulic conductivity of  $7.5 \times 10^{-7}$  cm/s according to falling-head permeameter tests of cores. Groundwater within 1–2 km of the bay is saline to a depth of at least 14 m (21), rendering source water separations based on salinity unreliable. In the rest of this paper the term “groundwater” refers to marsh plain and hyporheic pore waters.

The DTS cable was taped to plastic rope at 1-m intervals, allowing slight slack in the cable to relieve cable strain; it was then placed in a small, hand-dug trench in the channel bed and covered with  $\sim$ 3 cm of sediment. Every 2 m the rope was tacked to the channel bed with a 15-cm steel landscaping staple. Extra cable (170 m) was coiled above the reach of the tide with the ends in dry protective housings.

Additional data, logged at 1-min intervals, included the following: water table elevations, groundwater temperatures, tidal stage, tidal temperature, and supplementary channel-bed temperatures (Figure 1). A weather station was installed over a natural reference crop of saltmarsh vegetation less than 200 m from the study site. The station monitored the

following parameters every minute and recorded 10-min averages: air temperature and relative humidity, wind speed and direction, barometric pressure, precipitation, incoming shortwave solar radiation, and ground temperature at 30- and 50-cm depths. Bay water temperatures throughout the tidal cycle were obtained from the nearest NOAA tide station (22), which compared well with those measured during high tides at the main channel mouth.

## Results and Discussion

DTS data quality was assessed via multiple indicators. The signal loss reported by the DTS unit along the length of the cable was small ( $\sim$ 0.5 dB/km) and comparable to cable specifications. Noisy signal degradation due to end-reflection was confined to the first and last 10 m of cable, which were well outside the tidal channel study area. The DTS data resolved ice–water (0.4 and 0.6 °C) and surface water (16.9 and 18.1 °C) baths applied in the field to each end of the cable (south and north, respectively) within the precision of the instrument at the given averaging time. DTS measurements also corresponded well with supplementary bed temperatures monitored at 14 points (0.6% average deviation from HOBOS; locations in Figure 1).

The DTS data revealed the influences of warm tidal water, solar radiation, variable air temperatures, and the cool ground (Figure 2). The data showed that daytime high tides (DHTs) moderated channel bed temperatures by preventing intense radiative warming. Bed temperatures during DHTs exhibited strong day-to-day spatial consistency (correlation coefficient  $r = 0.89$  between the two days). Night-time high tide (NHT) bed temperatures were spatially similar to the DHTs ( $r = 0.70$ ), with differences driven by solar heating and similarities due to the relatively constant temperature of the bay water. The spatial structures of bed temperatures during the evening (ELT) and morning (MLT) low tides, when the channels were empty, were nearly identical ( $r = 0.95$ ). We found the spatial consistency between these temperature profiles (see Figure 3a and c), despite their separation by many hours of changing tidal and diurnal conditions, surprising; such repetition was suggestive of stable underlying physical causes. The rest of this paper describes in detail this thermal regime of consistent temperature anomalies and trends and discusses the underlying mechanisms.

Three types of temporally persistent bed temperature anomalies are visually manifest in Figure 2c and d as horizontal streaks: locations that were cooler on average at high tide but warmer during low tides (CH/WL), locations much warmer at low tide but not anomalous at high tide

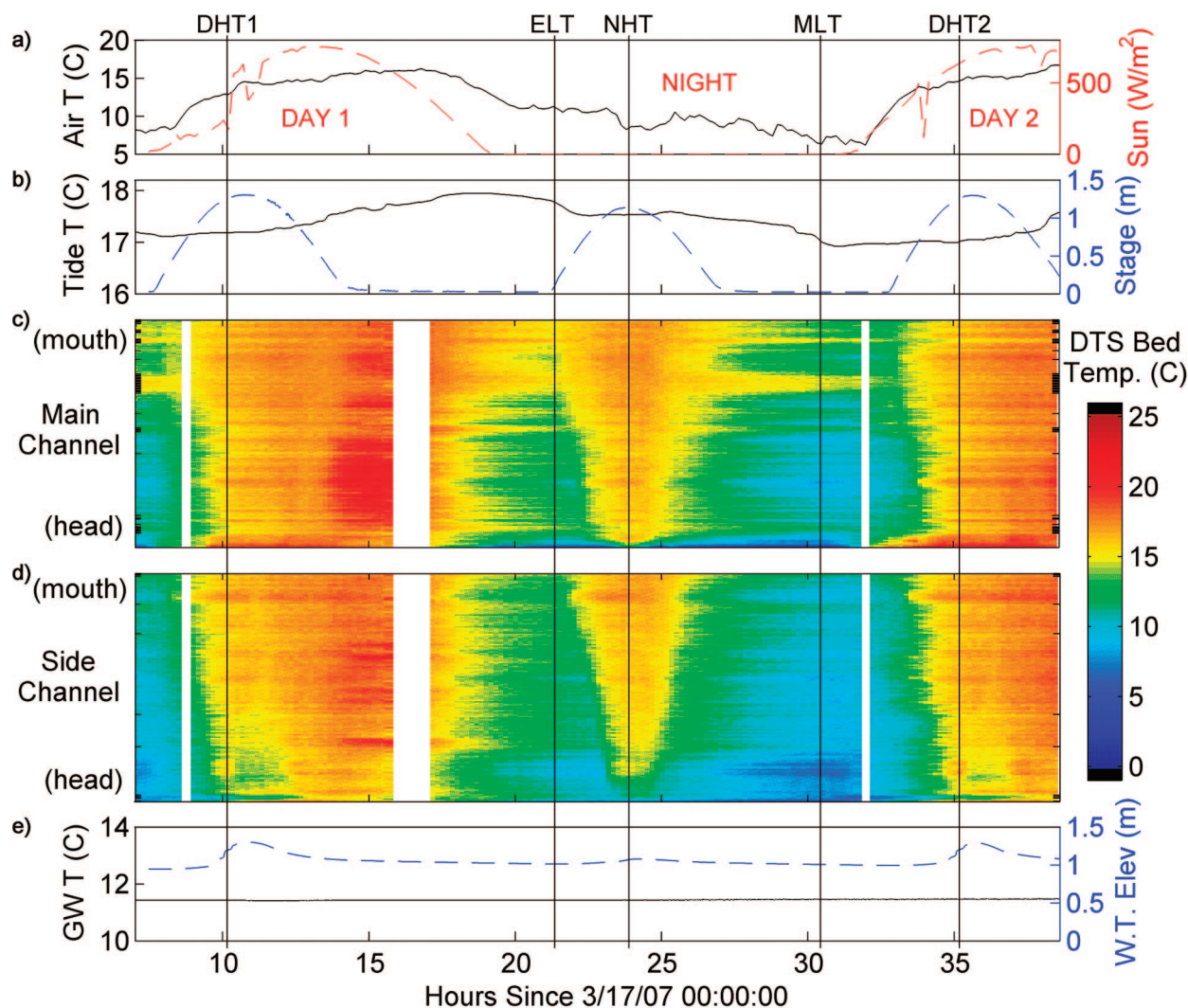


**FIGURE 2. Concurrent histories:** (a) air temperature (black) and solar radiation (red, dashed); (b) tide temperature (black) and tidal stage at main channel mouth (blue, dashed); DTS channel-bed temperatures in the (c) main and (d) side channels; (e) average groundwater temperature (black) and average water table elevation (blue, dashed). Tidal stage and water table elevation are in m-aMSL. Vertical white bars in (c) and (d) are periods of missing data. Vertical black lines mark times presented in Figure 3 as temperature profiles.

(WL), and locations that were warmer at high tide and cooler at low tide (WH/CL). Anomalies are also apparent in the temperature profiles of Figure 3a and c as spatially discrete peaks and valleys.

The anomalous temperatures of high-variance, WH/CL locations mirrored the tidal signal. We interpreted the cause of these anomalies to be shallow cable burial, more thermally conductive bed sediments, or both, such that the cable was in better-than-average contact with the warm overlying water at high tide and cool overlying air at low tide and so registered temperatures dominated by conductive heat exchange.

The thermal disparities of low-variance WL and CH/WL anomalies suggested more interesting underlying hydrologic causes. A metric was developed to extract these low-variance anomalies from the background temperature trends in the channels; it is summarized as a detrended mean absolute deviation, scaled by the sample variance, and is designated DEV:

$$DEV_i = \frac{\frac{1}{n} \sum_{t=1}^n |T_i^t - T_i^{*t}|}{\frac{1}{n-1} \sum_{t=1}^n (T_i^t - \bar{T}_i)^2}$$

Variables are as follows:  $n$  time steps in data; temperature  $T$  at location  $i$  and time  $t$ ; temperature  $T_i^{*t}$  predicted for location  $i$  by a least-squares fit to the temperatures in that channel (main or side) at time  $t$ . Temperature trends,  $T_i^*$ , are plotted as dotted lines in Figure 3a and c and are discussed in detail later in this paper. We define low-variance anomaly locations as occurring where  $DEV_i$  is greater-than-average

$$(DEV_i > \overline{DEV}; \overline{DEV} = 0.114);$$

20% of the 1-m channel reaches within our study meet this criterion (circled in blue in Figure 3b and d). These locations are indicated with tick marks on the y-axes of Figure 2c and d and as dark bars on the x-axes of Figure 3b and d.

An especially large, warm-low tide (WL) anomaly occurred along the eastern bank of the island surrounding Well J, 42–57 m from the main channel mouth (see Figure 3a). The water table elevation in Well J exhibited a maximum excursion of 30 cm below the ground surface, more than in any other well, while the temperature at the bottom of the well, at approximately the same depth as the bed of the adjacent main channel reach (1.3 m), remained constant. These data suggest that the WL anomaly resulted from delayed drainage of warm surface water introduced laterally at the water table

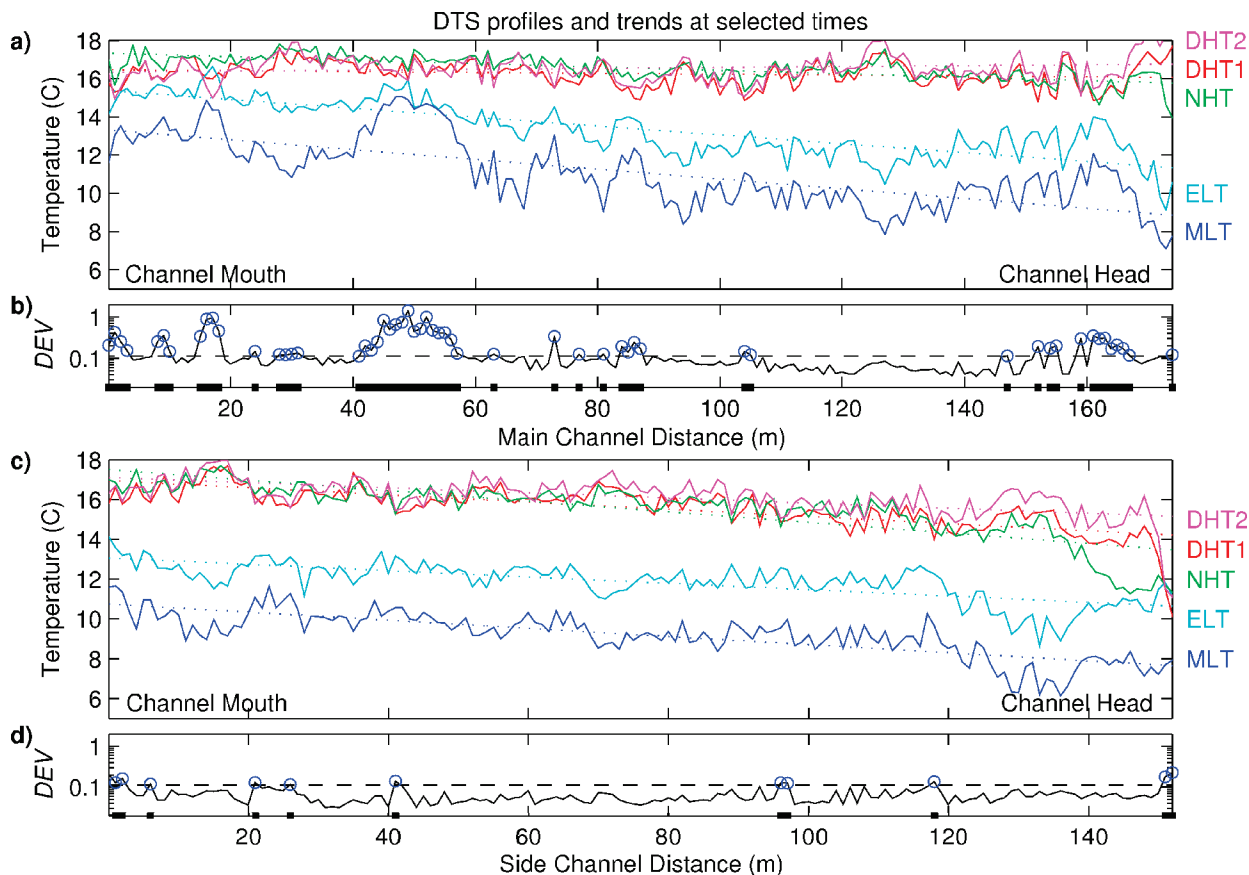


**FIGURE 3.** DTS temperature profiles and trends in the (a) main channel and (c) side channel at the selected times described in the text. Locations of low-variance WL and CH/WL anomalies, with  $DEV > 0.114$ , are denoted by thick lines along the (b) main and (d) side channels' distance axes.

into the channel bank during the previous high tide; this mechanism is consistent with literature on channel bank storage in tidal salt marshes (23). The large magnitude of this surface water–groundwater exchange feature may be due to locally higher hydraulic conductivities or improved drainage due to the island's geometry; its well-defined lateral extent and uniqueness among our data suggest that small-scale heterogeneity in exchange fluxes may be typical of tidal channel-bank systems.

The CH/WL anomalies point to a different source of thermal buffering that maintains more intermediate bed temperatures throughout the tidal cycle. Some of these locations coincided with microtributary locations known *a priori*. We hypothesized that the partial incision of a microtributary into the marsh plain allowed for the formation of a short but laterally extensive seepage face that drained cooler groundwater from the interior of the marsh; when a flood tide exceeded the elevation of the microtributary mouth, the warmer surface water filled the available bank storage capacity and also mixed with groundwater that had ponded in the microtributary channel. Microtributaries thus would facilitate mixing between surface water and groundwater and enhance drainage of mixed waters, which would then locally buffer bed temperatures in the primary channel as they slowly discharged. We subsequently located microtributaries at 80% of the low-variance anomaly locations identified by our DEV metric; the set of anomaly locations captured all especially wide and/or deep tributaries. In measuring channel bed temperature, the DTS data integrated the effects of upward exfiltration through the channel bed, ponding of bank seepage, and runoff of microtributary discharge; the remaining 20% of low-variance anomaly locations may have been dominated by the former two effects. We expect that the

unique thermal signature of CH/WL anomalies can, in general, be used to identify hidden, hydrologically significant microtributaries otherwise very difficult to locate beneath thickly matted coastal wetland vegetation cover.

Our data show for the first time the unique function of saltmarsh microtributaries as high-permeability conduits that facilitate groundwater–surface water mixing. The importance of microtributaries appears 2-fold: (a) microtributaries carry surface water further away from the main channel before it infiltrates into bank storage, resulting in longer residence times and greater mixing; and (b) infiltration into the microtributary banks far away from the main channel steepens the gradient toward the primary channel's seepage face during ebb tide, locally increasing groundwater discharge. Hence, microtributary-dependent exchange mechanisms operate on a broader scale than the local bank-exchange of which WL anomalies are symptomatic. This previously unrecognized component of the hydrologic system may help explain discrepancies between modeled and isotopically estimated saltmarsh groundwater discharge quantities (e.g., ref (23)).

In the background of the temperature anomalies we detected steep temperature gradients, trending from higher temperatures near the bay to lower temperatures inland in both channels (Figure 3a and c, dotted lines). The main channel exhibited steeper temperature gradients than the side channel during low tides; during high tides channel bed temperatures approached the surface water temperature. Averaged over the 1.3 tidal cycles of DTS data collection, main channel bed temperatures decreased 1.2 °C and side channel bed temperatures decreased 2.0 °C per 100-m distance inland. The maximum inland-decreasing gradients measured at any time were 3.2 °C/100-m in the main channel

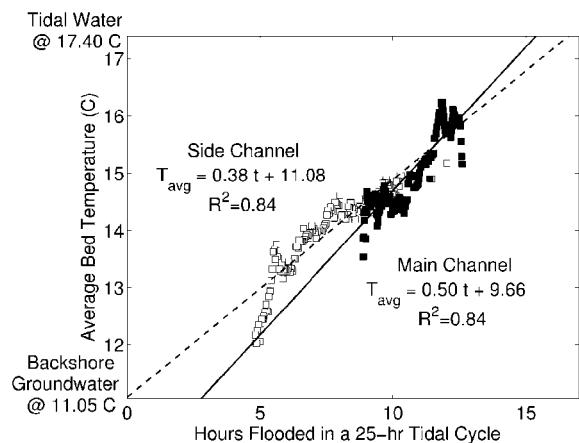


**FIGURE 4. Competition between warming tidal conduction and cold groundwater advection. Bed locations flooded longer have higher average temperatures: open squares/dotted line, side channel; filled squares/dashed line, main channel.**

**TABLE 1. Ambient Environmental Temperatures**

system component	average (°C)	range (°C)
bay water	17.40	16.92–17.94
marsh-plain groundwater	11.55	11.36–11.76
backshore groundwater (at Well B)	11.05	10.96–11.06
daytime air	14.65	8.30–17.22
night-time air	8.93	6.19–11.27
overall air	12.29	6.19–17.22

and 5.2 °C/100-m in the side channel, both within an hour before peak NHT.

We initially hypothesized that the bed temperature gradients were dominated by heat conduction from surface water, which would depend on the time a channel reach spent flooded; flood duration increased along each channel from its head to mouth. Figure 4 shows that the average bed temperatures in each channel exhibited linear mixing between a warm, often-flooded end-member and a codominant, cold, often-exposed end-member. Though the time that each location spent flooded accounted for 84% of the spatial variance in temperature, the large regressions' slopes ruled out simple dominance of bed temperatures by conduction from surface water. For convenience, we termed the warm end-member of this system, the proportionality between inundation time and the similarity between sediment and surface water temperatures, the "tidal thermal blanket effect".

To identify the cold end-member competing with the tidal thermal blanket effect we referred to ambient temperatures from the supplementary field data (Table 1): we noted that the side channel average temperature regression predicted a temperature of 11.08 °C for a channel location never flooded by the tide, similar to that of groundwater. In the main channel a similar extrapolation was less useful because the upper portion of the tidal range (flooded less than 9.0/25 h) was truncated at the backshore levee. Our data further support cold groundwater as the cold end-member of the system; we present the following two primary arguments and two supporting arguments. (Also see the Supporting Information.)

(1) Night-time channel bed temperatures reached peak values coincident with NHT, then declined steadily during ebb tide throughout the channels. The temperature decline cannot be explained by radiative heat loss from the bed sediments or conductive loss to the air while the bed remained insulated by

warm overlying water. The temperature decline is explained by the upward flow of cold groundwater: at NHT, discharge was partially suppressed by higher (tidal) heads at the discharge boundary and the resulting decreased hydraulic gradient; during ebb tide, groundwater more readily discharged and the bed temperatures reflected the increased flux of cold groundwater.

(2) During the low-tide period just prior to sunset on day one, the low angle of the sun put the channel in shade and so reduced the effects of radiative heating. Bed temperatures decreased upon shading and declined steadily until three hours after sunset, when the night-time flood tide occurred. Bed temperatures were colder than air temperatures by up to 3.0 °C during this period, so conductive heat losses from the bed to the air cannot explain the bed temperature decline. Because humidity in the moist channel was high and the channel was protected from wind, evaporative heat loss was negligible; a limiting calculation shows that evaporative heat loss (assuming complete wet bulb-depression) could only account for, at most, a 0.7–1.5 °C difference between bed and air temperatures. Therefore, cold groundwater discharge is the most plausible explanation for the sharp temperature decline registered by the DTS in the channel bed during this period.

(3) The inland-decreasing temperature gradients persisted throughout high tide, when the channel bed was thermally disconnected from the air's thermal mass for many hours (see Figures 2 and 3); in the absence of cold groundwater exfiltration, bed temperatures should instead have eventually equilibrated with the surface water.

(4) Average bed temperatures decreased sharply over a small interval of exposure time at the head of both channels (Figure 4), which is inconsistent with conduction from a relatively homogeneous air mass but consistent with our conceptual model of strongly gaining upper reaches of tidal channels.

The temperature trends within the DTS data thus revealed significant diffuse groundwater discharge throughout the channels during both high and low tidal stages. We emphasize that there was no reason to believe, *a priori*, that temporally averaged bed temperatures should be a linear function of exposure time. Complicating factors are thermally well-mixed tidal waters, variable air temperatures, the temporally exponential nature of heat conduction, the nonlinearity of radiative warming (combining solar, tidal, and shading effects), the combination of an harmonic tidal signal and an irregular channel elevation profile, and spatially variable bank storage and discharge (shown by our temperature anomaly analysis). The linear mixing relationship described by our data emphasizes the codominance of saltmarsh channel systems by both the tides and groundwater, with significance for studies of coastal groundwater discharge and near-shore biogeochemistry. This new conceptual model might also usefully inform siting of saltmarsh channel-bed benthic studies.

In drawing general conclusions about the effects of the tidal thermal blanket throughout the intertidal zone, a comparison between our results from saltmarsh tidal channels and the more well-established heat balance of intertidal mudflats (e.g., ref (13)) is instructive. Contrary to our decreasing-inland bed temperatures, Cho et al. (24) found increasing-inland temperatures across 1.5 km of intertidal mudflat sediments to a depth of at least 40-cm during a similar season in South Korea. The two seemingly contradictory results are both explained by the tidal thermal blanket effect: the difference in gradient direction is due to interaction between the tidal thermal blanket and different competing thermal end-members. Though ambient temperatures were not explicitly reported by Cho et al., we infer from their published data that on broad, low-relief intertidal mudflats the tidal thermal blanket competes with solar heating (see Supporting Information). The data of Cho et al. do not show a cooling effect due to groundwater discharge, likely pre-

vented by the extremely shallow slope of the system, but do show a gradient inversion from cold autumn temperatures and decreased solar radiation, consistent with our interpretation.

This comparison highlights just one difference between the thermal regimes of adjacent intertidal salt marsh and mudflat ecosystems: topography is the critical factor that moderates the relative influences of advection, radiation, and conduction via such mechanisms as the local hydraulic gradient, surface shading, and the inundation pattern. Large- and small-scale thermal patterns in the intertidal zone are diagnostic of spatial and temporal variations in these mechanisms. We identified thermal signatures representing three scales of surface water–groundwater exchange in salt marshes: localized channel bank storage-and-release of recent tidal waters, drainage of waters mixed over a meso-scale area by microtributaries, and diffuse groundwater discharge from the marsh as a whole that contributed to large-scale intertidal temperature gradients. Experimental detection of the latter two types of exchange for the first time was uniquely afforded by the exhaustive coverage of the DTS system.

DTS technology is well-suited to the study of dynamic environments such as the intertidal zone, where quickly changing conditions make spatially and temporally exhaustive data invaluable. Sudden changes in the thermal gradient across ecosystem boundaries, such as between salt marshes and mudflats, may not be uncommon and could be used in other systems as a diagnostic of tradeoffs between different dominant environmental forcing factors. The value to intertidal hydroecology of such large, but easily attainable, temperature data sets is an improved understanding of surface–subsurface exchanges and a new ability to identify anomalous temperature environments that might serve as thermal refugia within intertidal channels.

## Acknowledgments

This work was supported by the National Science Foundation under grant EAR-0634709 to Stanford University. The participation of Drs. Tyler, Torgersen, and Menon was supported in part by the U.S. Bureau of Reclamation. Dr. Selker's participation was supported by the National Science Foundation under grant EAR-0447415. Any opinions, findings, and conclusions or recommendations expressed in this material are those of the authors and do not necessarily reflect the views of the National Science Foundation. We gratefully acknowledge D. Anderson and D. Bartens of the City of Palo Alto Baylands Nature Preserve for their encouragement. We thank S. BeVillie, B. Ebel, C. Heppner, K. Knee, S. Loheide, H. Michael, M. Minihane, B. Mirus, M. Ronayne, V. Srinivasan, and K. Tufano for their field assistance. We also thank two anonymous reviewers.

## Supporting Information Available

List of equipment used, elaboration on detection of diffuse groundwater discharge, and details of interpretation of data from ref 24. This information is available free of charge via the Internet at <http://pubs.acs.org>.

## Literature Cited

- (1) Ataie-Ashtiani, B.; Volker, R. E.; Lockington, D. A. Tidal effects on groundwater dynamics in unconfined aquifers. *Hydrol. Processes* **2001**, *15*, 655–669.
- (2) Valiela, I.; Teal, J. M. The nitrogen budget of a salt marsh ecosystem. *Nature (London, U.K.)* **1979**, *280*, 652–656.
- (3) Testa, J. M.; Charette, M. A.; Sholkovitz, E. R.; Allen, M. C.; Rago, A.; Herbold, C. W. Dissolved iron cycling in the subtropical estuary of a coastal bay: Waquoit Bay, Massachusetts. *Biol. Bull.* **2002**, *203*, 255–256.

- (4) Ullman, W. J.; Chang, B.; Miller, D. C.; Madsen, J. A. Groundwater mixing, nutrient diagenesis, and discharges across a sandy beachface, Cape Henlopen, Delaware (USA). *Estuar. Coast. Shelf Sci.* **2003**, *57*, 539–552.
- (5) Windom, H.; Niencheski, F. Biogeochemical processes in a freshwater-seawater mixing zone in permeable sediments along the coast of Southern Brazil. *Mar. Chem.* **2003**, *83*, 121–130.
- (6) Moore, W. S.; Krest, J.; Taylor, G.; Roggenstein, E. Thermal evidence of water exchange through a coastal aquifer: implications for nutrient fluxes. *Geophys. Res. Lett.* **2002**, *29*, 1704.
- (7) Land, L. A.; Paull, C. K. Thermal gradients as a tool for estimating groundwater advective rates in a coastal estuary: White Oak River, North Carolina, USA. *J. Hydrol.* **2001**, *248*, 198–215.
- (8) Burnett, W. C.; Aggarwal, P. K.; Aureli, A.; Bokuniewicz, H.; Cable, J. E.; Charette, M. A.; Kontar, E.; Krupa, S.; Kulkarni, K. M.; Loveless, A.; et al. Quantifying submarine groundwater discharge in the coastal zone via multiple methods. *Sci. Total Environ.* **2006**, *367*, 498–543.
- (9) Banks, W. S. L.; Paylor, R. L.; Hughes, W. B. Using thermal-infrared imagery to delineate ground-water discharge. *Ground Water* **1996**, *34*, 434–443.
- (10) Duarte, T. K.; Hemond, H. F.; Frankel, D.; Frankel, S. Assessment of submarine groundwater discharge by handheld aerial infrared imagery: case study of Kaloko fishpond and bay, Hawai'i. *Limnol. Oceanogr. Meth.* **2006**, *4*, 227–236.
- (11) Loheide, S. P., II; Gorelick, S. M. Quantifying stream-aquifer interactions through the analysis of remotely sensed thermographic profiles and in situ temperature histories. *Environ. Sci. Technol.* **2006**, *40*, 3336–3341.
- (12) Robinson, C.; Li, L.; Barry, D. A. Effect of tidal forcing on a subtropical estuary. *Adv. Water Resour.* **2007**, *30*, 851–865.
- (13) Vugts, H. F.; Zimmerman, J. T. F. Interaction between the daily heat balance and the tidal cycle. *Nature (London, U.K.)* **1975**, *255*, 113–117.
- (14) Miller, D. C.; Ullman, W. J. Ecological consequences of ground water discharge to Delaware Bay, United States. *Ground Water* **2004**, *42*, 959–970.
- (15) Torgersen, C. E.; Price, D. M.; Li, H. W.; McIntosh, B. A. Multiscale thermal refugia and stream habitat associations of Chinook salmon in northeastern Oregon. *Ecol. Appl.* **1999**, *9*, 301–319.
- (16) Maragni, D. B. Chinook salmon. In *Baylands Ecosystem Species and Community Profiles: Life Histories and Environmental Requirements of Key Plants, Fish and Wildlife*; Report prepared by the San Francisco Bay Area Wetlands Ecosystem Goals Project; Olofson, P., Ed.; San Francisco Bay Regional Water Quality Control Board: Oakland, CA, 2000; pp 91–100.
- (17) South Bay Salt Pond Restoration Project: Biology and Habitats Existing Conditions Report, 2005. Available at <http://www.southbayrestoration.org>.
- (18) Selker, J. S.; Thévenaz, L.; Huwald, H.; Mallet, A.; Luxemburg, W.; van de Giesen, N.; Stejskal, M.; Zeman, J.; Westhoff, M.; Parlange, M. B. Distributed fiber-optic temperature sensing for hydrologic systems. *Water Resour. Res.* **2006**, *42*, W12202.
- (19) Selker, J.; van de Giesen, N.; Westhoff, M.; Luxemburg, W.; Parlange, M. B. Fiber optics opens window on stream dynamics. *Geophys. Res. Lett.* **2006**, *33*, L24401.
- (20) Hamlin, S. N. *Injection of Treated Wastewater for Ground-Water Recharge in the Palo Alto Baylands, California: Hydraulic and Chemical Interactions; Preliminary Report*; Water-Resources Investigation Report 82-4121; U.S. Geological Survey: Sacramento, CA, 1983.
- (21) Reymers, V.; Hemmeter, R.; Ahmadi, B., Eds. *Groundwater Conditions 2001*; Santa Clara Valley Water District: San Jose, CA, 2002.
- (22) Tides & Currents [Online]; Center for Operational Oceanographic Products and Services: Silver Spring, MD, 2007; Historic Tide Data (9414523 Redwood City, CA) [http://tidesandcurrents.noaa.gov/data\\_menu.shtml?type=Historic+Tide+Data&mstn=9414523](http://tidesandcurrents.noaa.gov/data_menu.shtml?type=Historic+Tide+Data&mstn=9414523) (accessed Apr 24, 2007).
- (23) Gardner, L. R. A modeling study of the dynamics of pore water seepage from intertidal salt marsh sediments. *Estuar. Coast. Shelf Sci.* **2005**, *62*, 691–698.
- (24) Cho, Y. K.; Kim, T. W.; You, K. W.; Park, L. H.; Moon, H. T.; Lee, S. H.; Youn, Y. H. Temporal and spatial variabilities in the sediment temperature on the Baeksu tidal flat, Korea. *Estuar. Coast. Shelf Sci.* **2005**, *65*, 302–308.

ES071309M